

Extremely Low Molecular Gas Content in the Vicinity of a Red Nugget Galaxy at $z = 1.91$

T. MORISHITA,¹ Q. D'AMATO,^{2,3} L. E. ABRAMSON,⁴ ABDURRO'UF,⁵ M. STIAVELLI,¹ AND R. A. LUCAS¹

¹Space Telescope Science Institute, 3700 San Martin Drive, Baltimore, MD 21218, USA; tmorishita@stsci.edu

²INAF/IRA, Istituto di Radioastronomia, Via Piero Gobetti 101, 40129, Bologna, Italy

³Dipartimento di Fisica e Astronomia dell'Università degli Studi di Bologna, via P. Gobetti 93/2, 40129 Bologna, Italy

⁴The Carnegie Observatories, 813 Santa Barbara Street, Pasadena, CA 91101, USA

⁵Institute of Astronomy and Astrophysics, Academia Sinica, Taipei 10617, Taiwan

Submitted to ApJ

ABSTRACT

We present Atacama Large Millimeter/submillimeter Array (ALMA) Band 5 observations of a galaxy at $z = 1.91$, GDS24569, in search of molecular gas in its vicinity via the [C I] 3P_1 - 3P_0 line. GDS24569 is a massive ($\log M_*/M_\odot = 11$) and passively evolving galaxy, and characterized by compact morphology with an effective radius of ~ 0.5 kpc. We apply two blind detection algorithms to the spectral data cubes, and find no promising detection in or around GDS24569 to projected distance of ~ 320 kpc, while a narrow tentative line (4.1σ) is identified at $+1200$ km/s by one of the algorithms. From the non-detection of [C I] in these deep data cubes, we place a 3σ upper limit on molecular hydrogen mass, $\sim 1.5 \times 10^9 M_\odot$, which converts to an extremely low gas-to-stellar mass fraction, $\lesssim 1\%$. In combination with a previous result of an insufficient number of surrounding satellite galaxies, it is suggested that GDS24569 is unlikely to experience significant size evolution via satellite mergers. We conduct a spectral energy distribution modeling by including optical-to-far-infrared data, and find a considerably high ($\sim 0.1\%$) dust-to-stellar mass ratio, ~ 10 - $100\times$ higher than those of local early-type galaxies. We discuss possible physical mechanisms that quenched GDS24569.

Keywords: galaxies: evolution – galaxies: formation

1. INTRODUCTION

The origin of the most massive galaxies in the local universe has been a long standing subject of galaxy evolution. From analysis of stellar populations and chemical abundances of local galaxies, it has been inferred that the most massive galaxies in the local universe completed their formation at redshift $z \gtrsim 2$ (Kauffmann et al. 2003; Thomas et al. 2003; Gallazzi et al. 2005; Treu et al. 2005; McDermid et al. 2015). Recent near-infrared (NIR) observations indeed found many distant galaxies to be already quenched, showing consistency with the quenching timeline inferred from local and low- z universe (Brammer et al. 2009; Marchesini et al. 2009; Muzzin et al. 2013; Tomczak et al. 2014).

Interestingly, a large fraction of high- z massive quenched galaxies are characterized by compact morphology (Cimatti et al. 2004; Daddi et al. 2005; Trujillo et al. 2007; Buitrago et al. 2008; Ichikawa et al. 2010; Cassata et al. 2011). While the average size of galaxies is smaller at that high redshift (Trujillo et al. 2006; Morishita et al. 2014; van der Wel et al. 2014), high resolution imaging by the Hubble Space Tele-

scope (HST) and the adaptive optics of ground based facilities revealed that some of them have even smaller radius compared to the local counterpart at a similar mass, by a factor of ~ 5 (van Dokkum et al. 2008; Damjanov et al. 2009; Szomoru et al. 2010). Given the absence of such a compact galaxy population in normal fields in the local universe (Shen et al. 2003; Taylor et al. 2010, but see Valentinuzzi et al. 2010 for their presence in dense fields), the transition of galaxies in the size-mass plane implies that many high- z compact galaxies would have to experience significant size evolution.

Various scenarios of significant size evolution for compact galaxies have been proposed in the past decade, including dry/wet, major/minor mergers (Khochfar & Silk 2006; Naab et al. 2007; Hopkins et al. 2009; Naab et al. 2009; Nipoti et al. 2009) and AGN feedback (Fan et al. 2008; Damjanov et al. 2009) (see Conselice 2014, for a thorough review). Among these scenarios, the dry minor merger scenario has been popularly discussed and taken as the most successful scenario in terms of its efficiency of size increase; surrounding satellite galaxies accrete to the central compact galaxy, without

disturbing the central core, and in this way it can efficiently evolve effective radii with a small increase of stellar mass (Naab et al. 2009; Hopkins et al. 2009; Oser et al. 2010; Trujillo et al. 2011), while not all of them may have to follow the same path (Nipoti et al. 2012; Newman et al. 2012). The resulting stellar populations and mass profiles from this inside-out evolution are in good agreement with findings at intermediate redshifts (van Dokkum et al. 2010; Patel et al. 2013; Morishita et al. 2015; Papovich et al. 2015) and for local massive galaxies (Belfiore et al. 2017; Ellison et al. 2018).

However, such an interpretation remains indirect, and the data still admit other scenarios. For example, such compact galaxies may not have to be the typical massive galaxy population at low redshift. In fact, there is a significant number of compact galaxies but more preferably in cluster environments (Valentinuzzi et al. 2010; Poggianti et al. 2013). It has also been proposed that the observed trend of average galaxy sizes reflects progenitor bias (e.g., Carollo et al. 2013; Fagioli et al. 2016), where large radius galaxies may appear at later time and drive apparent size evolution while high- z compact galaxies remain as they are.

Toward more direct understanding of their following evolutionary path, Mármol-Queraltó et al. (2012) studied satellite galaxies around massive galaxies to calculate possible size increase that would likely happen through accreting these satellite galaxies. Interestingly, their results indicated that the extant satellite galaxies are not enough to account for significant size evolution to the local relation. Furthermore, Morishita & Ichikawa (2016) studied a compact galaxy at $z = 1.91$, GDS24569, in deep HST images from the extreme deep field (XDF) project (Illingworth et al. 2016), to search for satellite galaxies around it down to $\log M_*/M_\odot \sim 7.2$. Their conclusion is that the number of satellites is not enough either, and extra mass increase by, e.g. additional star formation, is required for GDS24569 to be on the local size-mass relation.

This poses a question whether additional in-situ star formation is possible in such compact quenched galaxies. One missing key component in these studies is gas, in particular in the form of molecular hydrogen. While the stellar component is not enough for the mass increase required to be on the local relation, additional star formation caused by remaining or newly accreted gas could change their sizes significantly (i.e. the scenario C in Morishita & Ichikawa 2016).

To answer the question, we here present new observations with the Atacama Large Millimeter/submillimeter Array (ALMA) on GDS24569. Our configuration allows wide field-of-view (FoV) coverage to the extent of its virial radius, $r \sim 300$ kpc. Due to the spectral window available for the source redshift, we target atomic carbon, [C I] 3P_1 - 3P_0 (rest-frame frequency 492 GHz, hereafter [C I]), which is known

as a good alternative tracer of molecular hydrogen in extragalactic systems, originated from photodissociation regions.

The paper is constructed as follows. In Sec 2, we describe our observations and data reduction. In Sec 3, we present our analysis method of a blind search for gas in the ALMA data, and results. While the primary goal in this study is to search for surrounding gas, the dataset also provides us an opportunity to investigate the cause of quenching in the central galaxy from a panchromatic analysis over optical-to-far-infrared (FIR) wavelengths (Sec. 3.4). In Sec. 4, we discuss our results and present our interpretation. Throughout, magnitudes are quoted in the AB system assuming $\Omega_m = 0.3$, $\Omega_\Lambda = 0.7$, $H_0 = 70 \text{ km s}^{-1} \text{ Mpc}^{-1}$, and we assume the Salpeter (1955) initial mass function.

2. DATA AND ANALYSIS

2.1. Target galaxy

Our primary target, GDS24569, is a massive ($\log M_*/M_\odot \sim 11$) galaxy at $z = 1.91$, originally reported in Daddi et al. (2005). The galaxy is passively evolving, characterized by its spectral features, and has compact morphology with effective light radius ~ 0.5 kpc (Szomoru et al. 2010), which converts to stellar mass density of $\log \Sigma_*/M_\odot \text{ kpc}^{-2} \sim 11$ (Fig. 1). Morishita et al. (2019) analyzed its spectral energy distribution (SED) by fitting photometric and spectroscopic data points, and revealed that the galaxy experienced a very short period of star formation ~ 0.5 Gyr prior to its observed redshift, characterizing it as a quenched galaxy (see also Sec. 4).

On the size-mass plane, GDS24569 is located $\sim 2\sigma$ below the median size of passive galaxies at that redshift and stellar mass (van der Wel et al. 2014). To speculate its future evolutionary path, Morishita & Ichikawa (2016) investigated surrounding sources photometrically selected in extremely deep images from the XDF project (Illingworth et al. 2013), down to $\sim 10^8 M_\odot$. There are insufficient satellite galaxies to move GDS24569 onto the local size mass relation when following a simple formula for a minor merger scenario, $\Delta r \propto \Delta M^2$ (Naab et al. 2009). While GDS24569 may end up as one of the compact population found in the local universe, it is worth investigating any contribution from optically-dark components, which may trigger a significant starburst and size evolution before we conclude.

2.2. ALMA Cycle 7 observation

Interferometric observations with Band 5 were executed in ALMA cycle 7 (PID. 2019.1.01127.S, PI T. Morishita). We designed the observations so they would reveal gas components down to $\sim 10^8 M_\odot$ within the virial radius of GDS24569, ~ 300 kpc, via the [C I] emission line with an excitation temperature of ~ 30 K. Since our purpose here is not to resolve each gas clump, we optimize the antennas' con-

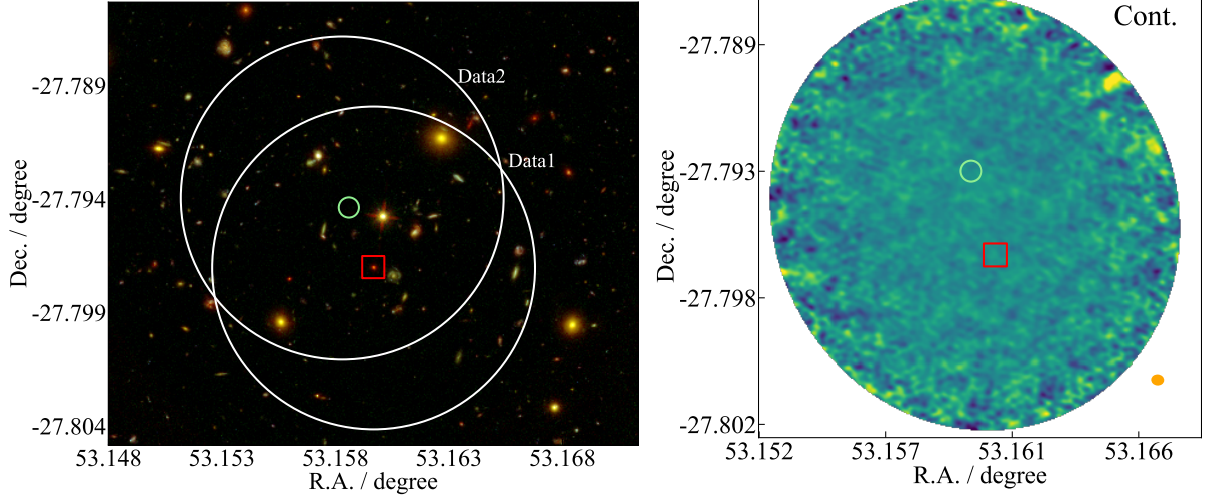


Figure 1. (Left): Pseudo RGB image (F160W+F814W+F435W of HST) of the observed field. The two ALMA pointings are overlaid (Data1 and Data2; white circles). The target, GDS24569, is centered in the image (red square). The position of the tentative detection found in Data2 (Sec. 3.2.2) is also shown (green circle), while no optical/IR counterpart is found at the position. (Right): Dust continuum map, created by collapsing the entire frequency range of the combined data cube. The coordinates of the objects in the left panel are indicated with the same symbols. No continuum emission is detected near the position of GDS24569. The beam size is shown at the bottom right (orange ellipse).

figuration for a large FoV, resulting in the final beam size of $1.0 \times 0.8 \text{ arcsec}^2$. We set three 1.875 GHz-width spectral windows, one of which was tuned to cover the [C I] frequency of the target ($\sim 169 \text{ GHz}$), while the other two spectral windows were centered on 168.5 GHz and 170.4 GHz for a continuum estimate.

Our observations, originally executed in November 2019 with on-source exposure of 107 minutes, were accidentally off the central pointing for $\sim 12 \text{ arcsec}$, while GDS24569 was still within the FoV (dubbed as Data2). The observations were compensated in January 2020, with the target in the center as it was originally planned (Data1). We therefore acquired two datasets with the same setup for frequency and exposure time as described above (Fig. 1), which allow us an independent check on possible detection (Sec. 3). We ran the tclean task of CASA on each of the datasets, with parameters of pixel scale 0.16 arcsec and velocity resolution element $\sim 28 \text{ km/s}$ ($\sim 15.6 \text{ MHz}$).

3. METHOD AND RESULTS

3.1. Dust Continuum Emission

In Fig. 1, we show a continuum map created by collapsing the spectral data cube over the entire velocity range, -4000 – 3000 km/s . No continuum source is detected near the position of GDS24569. Root-mean-squares (RMSs) are calculated by `imstat` of CASA; $27 \mu\text{Jy/beam}$ and $34 \mu\text{Jy/beam}$ for Data1 and Data2, respectively, and $21 \mu\text{Jy/beam}$ for the combined data cube at the target source position. This non-detection of dust emission is consistent with the optical-to-NIR SED analysis of GDS24569, $A_V \sim 0.4 \text{ mag}$ (Morishita

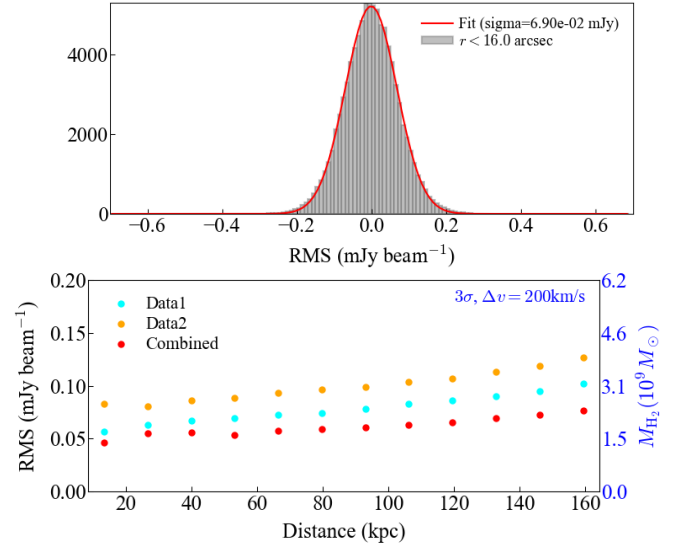


Figure 2. (Top): Distribution of fluxes measured at 1000 random positions in one of the data cubes. Fluxes are in units of mJy per beam per spectral element. (Bottom): Radial distribution of RMSs estimated at each radius in the three data sets — Data1 (cyan), Data2 (yellow), and combined (red) cubes. Corresponding molecular hydrogen mass limits (3σ) for a line width of $\Delta v = 200 \text{ km/s}$ are shown in the right y-axis.

et al. 2019). We will use the upper limit derived here for a panchromatic analysis in Sec. 4.

3.2. Clump Finding Algorithm

Our primary goal in this study is to search for gas clumps in the data cubes via the [C I] emission line, both in the position of GDS24569 and its neighboring regions out to $r \sim 300 \text{ kpc}$,

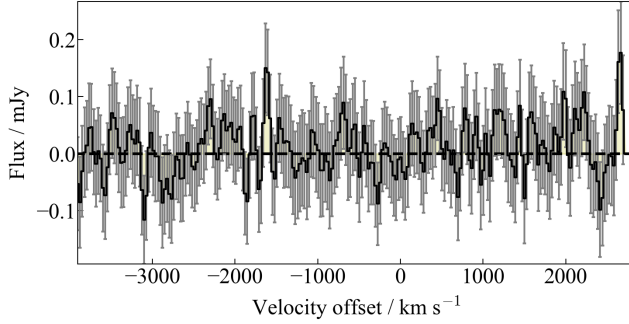


Figure 3. Spectrum extracted in the position of GDS24569 in the combined data cube, with an aperture of the beam size. No significant flux excess is seen.

which is its approximate virial radius. Despite a complicated aspect of blind detection in interferometric data cubes, our advantage is that we have two independent data cubes, so that any detection found in one data cube can be checked in the other. We start with a fiducial detection algorithm, `clumpfind` (Williams et al. 1994), but also apply a method introduced in D’Amato et al. (2020) to check the consistency.

3.2.1. Starlink Clumpfind Algorithm

To search for line detection across the data cubes, we apply an automated detection algorithm. We first run the `clumpfind` algorithm, implemented in the `starlink` package (Currie et al. 2014). One of the parameters for `clumpfind` is the noise level of the data represented by RMSs. While `imstat` of CASA provides a RMS value at each frequency value, the noise is correlated significantly for our case with a relatively large beam size. Furthermore, the data show differential noise structure along the radial direction from the center, where larger noise structures frequently appear at a larger radius. To estimate a more realistic noise level, we extract apertures of beam size in 1000 randomly selected positions in each cube, to measure RMSs in annuli at every 10 pixels from the center. As an example, the distribution of extracted fluxes is shown in the top panel of Fig. 2, where the distribution is well fitted with a Gaussian. A radial distribution of derived RMSs ($= \text{FWHM}/2.355$ of Gaussian fit) are shown in the bottom panel of Fig. 2. The RMS varies from $\sigma \sim 45 \mu\text{Jy}/\text{beam}/\text{spectral element}$ at the innermost region to $130 \mu\text{Jy}/\text{beam}/\text{spectral element}$ at the outermost region.

We run the `clumpfind` algorithm on each of two data cubes with various RMSs taken from the estimated range above. Other configuration parameters are also determined through our initial tests (`VELORES`=5, `MINPIX`=50, and `FWHM-BEAM`=3). With the setup, the algorithm initially detects ~ 100 sources from the entire FoV of each dataset for different RMS values. However, most of the identified clumps are located at outer regions, $r \gtrsim 15$ arcsec. Our visual inspection does not confirm any of these clumps as real sources.

Furthermore, none of these sources are commonly identified in both of the data cubes. We thus conclude that all of the detected clumps are artifacts. To confirm this, we also apply the same method to the data cubes but with signs of fluxes inverted. We find a similar number of detections with a similar spatial distribution as for the real cubes.

The spectrum extracted from the position of GDS24569 in the combined cubes is shown in Fig. 3. No obvious line is detected beyond the noise limit associated with each spectral element.

3.2.2. D’Amato et al. (2020)’s method

To double-check the non-detection in Sec. 3.2.1, we also apply a blind detection method introduced in D’Amato et al. (2020), that relies on spectral, spatial and reliability criteria.

We perform the detection on the signal-to-noise-ratio (S/N -) cube. In order to produce it, we firstly generate a noise-cube, where the pixels have the value of the RMS in a box centered in them. We choose a box with an area equal to that of 10 beams, since we find that this size allows us to trace the local variation of the noise in each channel, still having enough statistics per box. The RMS is recursively calculated to convergence masking all pixels above $3 \times \text{RMS}$ at each iteration. The S/N -cube is then obtained as the ratio between the original data-cube and the noise cube.

In order to perform the detection, we firstly scan each spaxel searching for a given amount of contiguous channels (N_{ch}) above a given S/N threshold. We search for $N_{\text{ch}}=2, 3, 4, 5$ (corresponding to $\sim 60, 90, 120, 150 \text{ km/s}$, respectively) above a S/N threshold of 1.5, 2, 2.5 and 3. Then, among the candidate detections, we reject all those with a number of contiguous pixels lower than a given amount N_{ch} . For each combination of N_{ch} and S/N threshold, we try $N_{\text{px}} = 2, 3, 4$.

Finally, in order to estimate the incidence of spurious detections, we perform the same algorithm on the “negative” S/N -cube, where the pixels have the same value and inverted sign of the original (“positive”) S/N -cube. Then, for any combination of N_{ch} , S/N threshold and N_{px} we reject all the candidate detections obtained from the positive S/N -cube that have a peak S/N lower than the maximum peak S/N of the detections obtained from the negative S/N -cube using the same parameter combination. Finally, we crop the detection area to the half-primary-beam-width.

From this analysis, we find one tentative detection (4.1σ) at $+1200 \text{ km/s}$ at projected distance $\sim 14 \text{ kpc}$ away from GDS24569 in Data2 (top panel of Fig. 4). The line is narrow, and fitted with a gaussian of $\text{FWHM} = 84 \text{ km/s}$ (~ 3 spectral elements). The total flux from the integral of the gaussian fit is $S_{\text{C I}} \Delta v \sim 7.5 \text{ mJy km/s}$. However, the line is not detected at the same spectral position in Data1, which is ~ 10.5 arcsec away from the center (bottom panel of Fig. 4). This may be attributed to lower sensitivity at the position in

Data1. We therefore leave this detection as tentative, while including this emission would not change our main conclusion in Sec. 4.

3.3. Upper limits in molecular gas mass

In this subsection, we attempt to place an upper limit on molecular hydrogen mass from the estimated RMSs in Sec. 3.2.1. Following a recipe by Papadopoulos et al. (2004, also Wagg et al. 2006; Man et al. 2019), molecular hydrogen gas mass is inferred by:

$$M_{\text{H}_2} = 1375.8 \frac{D_l^2}{(1+z)} \left(\frac{X[\text{C I}]}{10^{-5}} \right)^{-1} \times \left(\frac{A_{10}}{10^{-7} \text{s}^{-1}} \right)^{-1} Q_{10}^{-1} \frac{S_{[\text{C I}]} \Delta v}{\text{Jy km s}^{-1}} M_{\odot}. \quad (1)$$

The equation consists of two steps: conversion from observed [C I] intensity to atomic carbon mass, and then to molecular hydrogen mass. The conversion involves a couple of parameters. We adopt the excitation factor $Q_{10} = 0.5$ as a fiducial value, assuming local thermodynamic equilibrium (i.e. optically thin). Q_{10} ranges from 0 to 1, depending on the temperature, density and radiation field, though none of these values can be constrained without line ratios to other excitation levels. We adopt a molecular [C I]-to- H_2 conversion factor, $X[\text{C I}] = 5 \times 10^{-5}$ following the median value in Weiß et al. (2005). The conversion factor is known to be as low as $\sim 2 \times 10^5$ (Frerking et al. 1989; Weiß et al. 2003; Jiao et al. 2019), and thus our choice of Weiß et al. (2005)’s value gives a conservative upper limit. The conversion to molecular hydrogen mass includes the mass in Helium by a correction factor of 1.36 (Solomon & Vanden Bout 2005). $A_{10} = 7.93 \times 10^{-8} \text{s}^{-1}$ is the Einstein A-coefficient, and D_l is the luminosity distance to the source redshift, $z = 1.91$.

Since our input for the equation above is the upper limit for flux density, we need to assume the line width to obtain a velocity-integrated line intensity, $S_{[\text{C I}]} \Delta v$. We set $\Delta v = 200 \text{ km/s}$ as a typical line width from the literature (Weiß et al. 2005; Man et al. 2019), from which we obtain $S_{[\text{C I}]} \Delta v \sim 28 \text{ mJy km/s/beam}$ as a 3σ upper limit in the position of GDS24569. By substituting this in the equation above, we obtain an upper limit on molecular hydrogen mass to $\sim 1.5 \times 10^9 M_{\odot}$, characterizing a significantly low gas mass fraction, $\lesssim 1\%$. For the tentative line we found in Sec. 3.2.2, the same conversion provides $\sim 4 \times 10^8 M_{\odot}$, which is much smaller than a 3σ detection limit at this position ($\sim 2 \times 10^9 M_{\odot}$; see the bottom panel in Fig. 2), due to its narrow line width.

3.4. Panchromatic analysis of GDS24569

Morishita et al. (2019) investigated the star formation history of GDS24569 from a combined dataset of NIR spectrum and optical-to-NIR broadband photometry. We re-fit

the dataset with a SED fitting code, *gsf* (ver.1.4). From Morishita et al. (2019), we retrieve broadband photometry of HST and Spitzer up to IRAC CH4, originally published by the 3D-HST team (Skelton et al. 2014). Deep spectra of WFC3-IR G102 and G141 presented in Morishita et al. (2019) are also included, which are critical to constrain its stellar populations and star formation history.

We include the upper limit on the continuum obtained from our ALMA observations (Sec. 3.1). We also include Spitzer MIPS $24\mu\text{m}$ flux from Whitaker et al. (2014), and upper limits on MIPS $70\mu\text{m}$, Herschel PACS 100 and $160\mu\text{m}$ from the GOODS Herschel program (Elbaz et al. 2011). The broadband photometric data points used here are summarized in Table 1.

Following Morishita et al. (2019), we use synthetic spectral templates generated by *fsps* (Conroy et al. 2009), based on the MILES spectral library with the Salpeter (1955) initial mass function, with age pixels of $[0.01, 0.03, 0.1, 0.3, 0.5, 0.7, 1.0, 1.5, 2.0, 3.0] \text{ Gyr}$, and metallicity of $[-0.8, 0.6] / \log Z_{\odot}$, the same parameter setups as in Morishita et al. (2019). The Calzetti et al. (2000) dust attenuation model is adopted. We calculate FIR dust emission templates based on the recipe provided by Draine & Li (2007). Due to the limited number of FIR data points, we limit the calculation to their LMC model with $q_{\text{PAH}} = 2.37\%$.

In Fig. 5, we show the best-fit SED and star formation history of GDS24569. The result indicates that GDS24569 had the last primary star formation activity $\sim 0.5 \text{ Gyr}$ ago, and then rapidly declined its star formation activity by $\sim 100 \text{ Myr}$ before the observed redshift. Such a star formation history is in fact speculated from the absence of significant flux at rest-frame UV wavelength, as well as deep 4000 \AA break and Balmer absorption lines seen in the deep grism spectra, characterizing GDS24569 as a post-starburst galaxy (Dressler & Gunn 1983). Such rapid decrease in star formation activity is also seen in other massive galaxies (Belli et al. 2019; Morishita et al. 2019), while their primary quenching process remains unclear. The low gas fraction and the inferred dust mass of the system found in this study potentially add further constraints on the primary quenching mechanism (Sec. 4).

It is worth noting that the derived metallicity of GDS24569, $\log Z_{*}/Z_{\odot} \sim -0.2 \text{ dex}$, is $\sim 0.4 \text{ dex}$ below the mean relation of massive, non-compact quenched galaxies at $z \sim 2$ (Morishita et al. 2019). While the statistical significance is still small due to the scatter around the mean relation ($\Delta \sim 0.2 \text{ dex}$), this may further provide us a hint to its following evolution; if GDS24569 is representative of the compact galaxy population at this redshift, then a similarly low metallicity trend may be seen in local compact galaxies. Such a low metallicity implies that GDS24569 presumably experienced star formation of a short timescale in a relatively

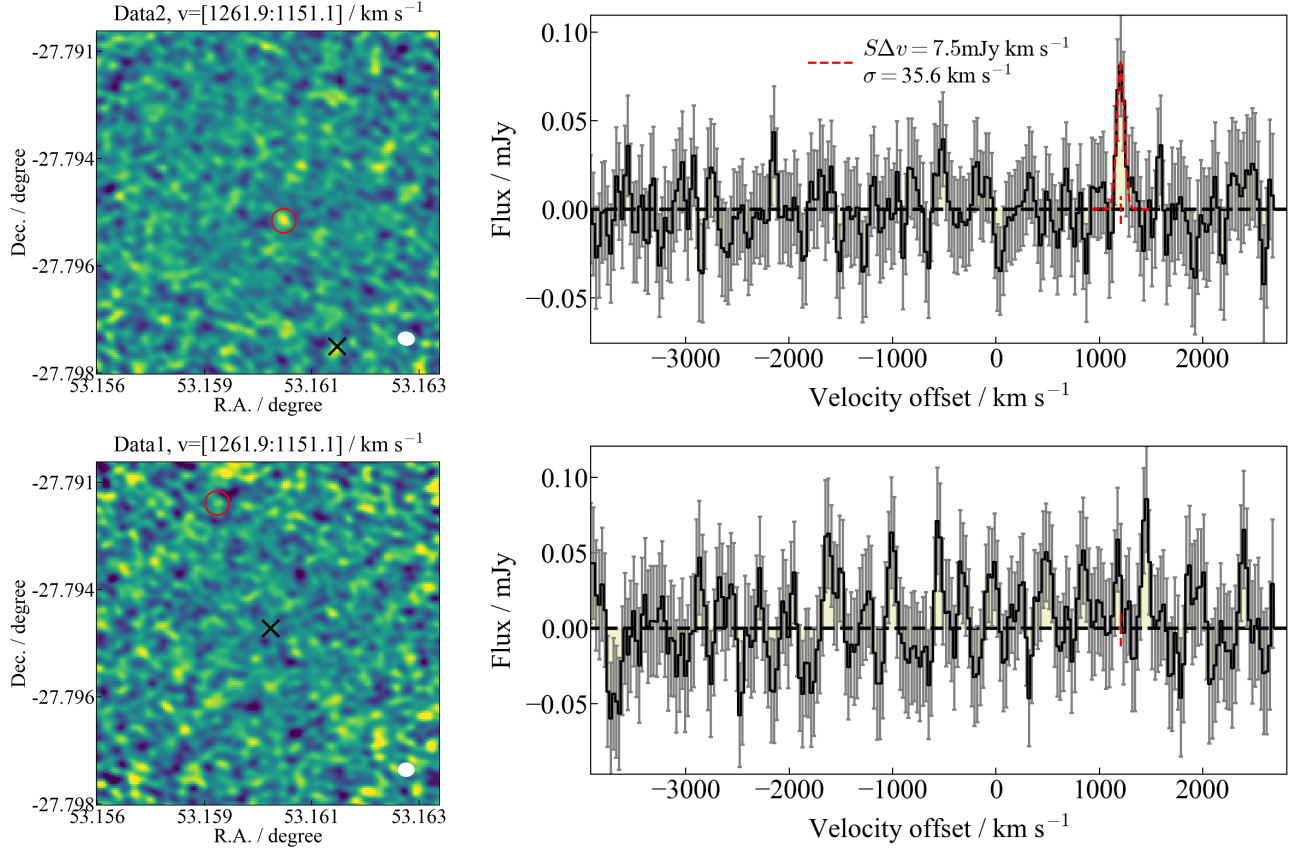


Figure 4. (Top): Tentative line detection at $V \sim 1200 \text{ km/s}$ in Data2 is shown (left panel; red circle) in the velocity integrated map (centered on its pointing). The position of GDS24569 is also shown (black cross). The beam size is shown at bottom-right (white ellipse). The Gaussian fit to the tentative line is overlaid in the extracted spectrum (right panel; red dashed line). (Bottom): Same as above but for Data1. No significant flux excess is seen at the velocity (red dashed line).

pristine gas environment (e.g., Kriek et al. 2016, see also below).

The best-fit result returns dust mass $\log M_{\text{dust}}/M_{\odot} = 7.8 \pm 0.8$, which derives its dust-to-stellar mass ratio $M_{\text{dust}}/M_{*} \sim 0.1\%$. While the data point of ALMA Band 5 is an upper limit, strong flux excess at $24\mu\text{m}$ constrains the FIR component sufficiently well. The inferred fraction is much higher than those of local early-type galaxies, ranging from $M_{\text{dust}}/M_{*} \sim 10^{-6}$ to 10^{-5} (Smith et al. 2012; Lianou et al. 2016), while a similar value was found from the stacking analysis of massive galaxies at $z \sim 1.8$ in Gobat et al. (2018). Such a significant amount of dust may play a critical role in suppressing star-formation activity, by preventing formation of hydrogen molecules (e.g., Kajisawa et al. 2015; Conroy et al. 2015). Our finding of the low gas mass fraction derived above is consistent with this scenario.

Our estimate of dust mass is robust to different assumptions in the SED modeling. We also fit our photometric data points with another SED fitting code, `pixelfit` (Abdurro’uf et al., in prep.), which adopts broader parameter ranges for the dust component. The code returns

$\log M_{\text{dust}}/M_{\odot} = 8.2^{+0.4}_{-0.6}$, in good agreement with the dust mass estimate by `gsf`.

No X-ray counterpart is found in the Chandra 7M sec catalog (Luo et al. 2017) at the positions of GDS24569 or the tentative line in Sec 3.2.2. The non-detection is reasonable given its passively evolving nature inferred from the SED and undisturbed morphology.

4. DISCUSSION AND SUMMARY

In this study, we investigated the vicinity of a massive compact galaxy, GDS24569, for molecular gas that can induce star formation and lead to strong size evolution to the local size-mass relation. Our two independent algorithms on the unique data cubes did not confidently detect any gas clumps or continuum emission, placing a conservative upper limit on molecular hydrogen mass. The result leads to the conclusion that GDS24569 is unlikely to be on the size relation of the early-type galaxies, at least via minor mergers, which is a popularly discussed evolutionary path (Naab et al. 2009; Oser et al. 2010). According to the analysis presented in Morishita & Ichikawa (2016, their Fig.4), if all satellite galaxies found in their deep images are to accrete, GDS24569 is able to in-

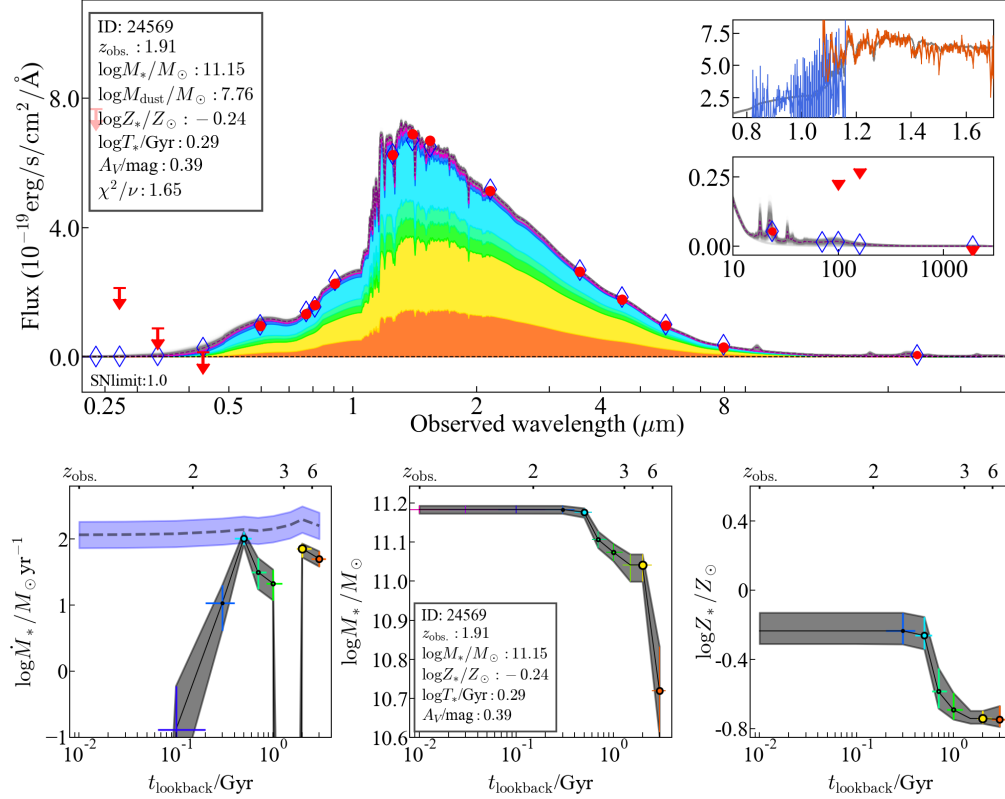


Figure 5. (Top): Spectral energy distribution (SED) of GDS24569. Broadband photometry (red points for detection and arrows for upper limits) from rest-frame UV to FIR (inset at right middle) and NIR grism spectra (inset at right top; red and blue lines for G141 and G102, respectively) are included. Flux contribution from each lookback time is shown with different colors (filled regions), whereas the best-fit total flux is shown with a dashed line (purple, with uncertainty in gray). (Bottom): Star formation (left), mass accumulation (middle), and metallicity evolution (right) histories of GDS24569. Colors of symbols at each lookback time correspond to those of spectral templates in the SED plot above. The star formation rate of the star-forming main sequence for a given stellar mass at each lookback time (Speagle et al. 2014) is shown in the left panel (dashed line with blue hatch).

crease its size by a factor of ~ 5 at most, which is still $\sim 2\sigma$ below the local size-mass relation of early-type galaxies at $z \sim 0$ (e.g., Shen et al. 2003; Taylor et al. 2010; Poggianti et al. 2013). Since most of their satellite galaxies are not spectroscopically confirmed, this extrapolation is rather optimistic and the actual size evolution can be even less significant.

In the local universe, on the other hand, there are a portion of compact, passively evolving galaxies in *high-density* regions i.e. in galaxy clusters (e.g., Valentinuzzi et al. 2010). These local compact galaxies, characterized by a similar light profile as for high- z compact galaxies, dominate a significant fraction of cluster member galaxies at $> 3 \times 10^{10} M_\odot$, $\sim 22\%$ (Valentinuzzi et al. 2010), whereas only $\sim 4.4\%$ in general fields (Poggianti et al. 2013). These findings imply insignificant size evolution of (at least) some of compact galaxies at high redshift, as is found in simulations (e.g., Wellons et al. 2016). Poggianti et al. (2013) also found that compact galaxies in dense environments consist of older stellar populations than those in general fields.

From these findings above, it is implied systematically earlier evolution of compact galaxies in dense fields, which is suggested by Morishita et al. (2017) and Abramson & Morishita (2018) from their structural analysis on cluster and field galaxies, as well as by direct comparison of stellar age of massive galaxies at $z \sim 2$ (Wu et al. 2018; Estrada-Carpenter et al. 2020). In fact, the stellar metallicity of GDS24569 implied from our SED fitting analysis is ~ 0.4 dex below the average trend of non-compact galaxies at the same redshift. Assuming that GDS24569 is representative of the progenitor population of local compact galaxies, then we may see systematical differences in their metallicity and chemical composition from those of other non-compact galaxies. While Taylor et al. (2010) found no significant metallicity offset of compact galaxies in general fields, currently such systematic comparison of local compact galaxies in dense environments has not been established.

Lastly, we revisit possible quenching mechanisms that could occur in GDS24569. Our observations found an extremely low gas mass fraction in the system, $\lesssim 1\%$, whereas the fraction ranges from $\sim 50\%$ to $\sim 100\%$ for the main se-

quence star-forming galaxies at similar redshifts (Daddi et al. 2010; Tacconi et al. 2018; Hayashi et al. 2018). Such a low gas mass fraction of passive galaxies is not a surprise. For example, Bezanson et al. (2019) reported a conservative upper limit of $\lesssim 7\%$ in a galaxy at $z = 1.522$. Furthermore, the extremely low gas fraction of GDS24569 is worth comparing with those of compact galaxies *at an earlier phase*, or blue nuggets (Barro et al. 2013; Williams et al. 2014; van Dokkum et al. 2015). Barro et al. (2017) reported a short depletion time (~ 27 Myr) of a star-forming compact galaxy at $z = 2.3$ from their CO observations with ALMA. The galaxy is intensively forming stars at $\sim 500 M_{\odot}/\text{yr}$, which is somewhat comparable to the peak star formation rate of GDS24569 (Fig. 5).¹ From this perspective, gas depletion by the past intense star formation activity can reasonable be considered as the primary cause of quenching for GDS24569.

We did not find gas clumps, disturbed gas structure, or dust emission in and around GDS24569. Given that the last primary star forming activity occurred relatively recently (~ 0.5 Gyr), this suggests that the past star formation activity was at least not caused by a galaxy-galaxy scale merger, and that gas was consumed inside the system rather than being ejected. This is consistent with a scenario derived from the local galaxies using stellar metallicity as an indicator (Peng et al. 2015). It is yet unclear what caused such intense star formation from our study. For example, Talia et al. (2018) observed an AGN-hosting compact star forming galaxy, and

concluded that the star formation is likely caused by positive feedback from the AGN activity. This positive feedback scenario seems possible given a higher fraction of compact star forming galaxies host AGN than the overall star-forming population (e.g., Kocevski et al. 2017; Wisnioski et al. 2018). On the other hand, such high efficiency in star formation can also be induced without AGN activity (Dekel & Burkert 2014; Semenov et al. 2018), leaving the conclusion still pending.

Given that the scenarios above are derived from one galaxy, we are still far from getting a general consensus on primary quenching mechanisms in compact massive galaxies. Nonetheless, in this study we showed that even non-detection of molecular gas and dust emission, in combination with a wide wavelength data coverage, sheds light on the nature of high- z passive galaxies. Application of this new approach to archival data will immediately improve statistical arguments.

ACKNOWLEDGEMENTS

T.M. is grateful to Kate Rowlands and Takuya Hashimoto for helpful discussion and advice on ALMA data reduction.

Software: Astropy (Astropy Collaboration et al. 2013, 2018), numpy (Oliphant 2006; Van Der Walt et al. 2011), python-fsps (Foreman-Mackey et al. 2014), EMCEE (Foreman-Mackey et al. 2013).

REFERENCES

- Abramson, L. E., & Morishita, T. 2018, *ApJ*, 858, 40
- Astropy Collaboration, Robitaille, T. P., Tollerud, E. J., et al. 2013, *A&A*, 558, A33
- Astropy Collaboration, Price-Whelan, A. M., SipHocz, B. M., et al. 2018, *aj*, 156, 123
- Barro, G., Faber, S. M., Pérez-González, P. G., et al. 2013, *ApJ*, 765, 104
- Barro, G., Kriek, M., Pérez-González, P. G., et al. 2017, *ApJL*, 851, L40
- Belfiore, F., Maiolino, R., Tremonti, C., et al. 2017, *MNRAS*, 469, 151
- Belli, S., Newman, A. B., & Ellis, R. S. 2019, *ApJ*, 874, 17
- Bezanson, R., Spilker, J., Williams, C. C., et al. 2019, *ApJL*, 873, L19
- Brammer, G. B., Whitaker, K. E., van Dokkum, P. G., et al. 2009, *ApJL*, 706, L173
- Buitrago, F., Trujillo, I., Conselice, C. J., et al. 2008, *ApJL*, 687, L61
- Calzetti, D., Armus, L., Bohlin, R. C., et al. 2000, *ApJ*, 533, 682
- Carollo, C. M., Bschorr, T. J., Renzini, A., et al. 2013, *ApJ*, 773, 112
- Cassata, P., Giavalisco, M., Guo, Y., et al. 2011, *ApJ*, 743, 96
- Cimatti, A., Daddi, E., Renzini, A., et al. 2004, *Nature*, 430, 184
- Conroy, C., Gunn, J. E., & White, M. 2009, *ApJ*, 699, 486
- Conroy, C., van Dokkum, P. G., & Kravtsov, A. 2015, *ApJ*, 803, 77
- Conselice, C. J. 2014, *ARA&A*, 52, 291
- Currie, M. J., Berry, D. S., Jenness, T., et al. 2014, in *Astronomical Society of the Pacific Conference Series*, Vol. 485, *Astronomical Data Analysis Software and Systems XXIII*, ed. N. Manset & P. Forshay, 391
- Daddi, E., Renzini, A., Pirzkal, N., et al. 2005, *ApJ*, 626, 680
- Daddi, E., Bournaud, F., Walter, F., et al. 2010, *ApJ*, 713, 686
- D’Amato, Q., Gilli, R., Prandoni, I., et al. 2020, *A&A*, 641, L6
- Damjanov, I., McCarthy, P. J., Abraham, R. G., et al. 2009, *ApJ*, 695, 101
- Dekel, A., & Burkert, A. 2014, *MNRAS*, 438, 1870
- Draine, B. T., & Li, A. 2007, *ApJ*, 657, 810
- Dressler, A., & Gunn, J. E. 1983, *ApJ*, 270, 7

¹ Our SFR estimates are time-averaged at each pixel, and actual values could be higher if star formation activity is more instantaneous.

Table 1. Photometric fluxes of GDS24569, in units of μJy .

F125W	F140W	F160W	F225W	F275W	F336W	F435W	F606W	F775W	F814W	F850LP
K_S	IRAC CH1	IRAC CH2	IRAC CH3	IRAC CH4	MIPS $24\mu\text{m}$	MIPS $70\mu\text{m}$	PACS $100\mu\text{m}$	PACS $160\mu\text{m}$	ALMA Band 5	
3.26 ± 0.02	4.49 ± 0.03	5.30 ± 0.03	< 0.14	< 0.05	< 0.03	< 0.01	0.11 ± 0.01	0.26 ± 0.01	0.35 ± 0.01	0.62 ± 0.02
7.99 ± 0.09	11.18 ± 0.07	11.98 ± 0.06	10.65 ± 0.42	6.09 ± 0.44	9.84 ± 2.72	< 8538.11	< 2203.38	< 6610.15	< 21.40	

NOTE— 1σ errors are quoted for those with $S/N > 1$, and 1σ upper limits for the rest of the data points.

Elbaz, D., Dickinson, M., Hwang, H. S., et al. 2011, *A&A*, 533, A119

Ellison, S. L., Sánchez, S. F., Ibarra-Medel, H., et al. 2018, *MNRAS*, 474, 2039

Estrada-Carpenter, V., Papovich, C., Momcheva, I., et al. 2020, *ApJ*, 898, 171

Fagioli, M., Carollo, C. M., Renzini, A., et al. 2016, *ApJ*, 831, 173

Fan, L., Lapi, A., De Zotti, G., & Danese, L. 2008, *ApJL*, 689, L101

Foreman-Mackey, D., Hogg, D. W., Lang, D., & Goodman, J. 2013, *PASP*, 125, 306

Foreman-Mackey, D., Sick, J., & Johnson, B. 2014, doi:10.5281/zenodo.12157

Frerking, M. A., Keene, J., Blake, G. A., & Phillips, T. G. 1989, *ApJ*, 344, 311

Gallazzi, A., Charlot, S., Brinchmann, J., White, S. D. M., & Tremonti, C. A. 2005, *MNRAS*, 362, 41

Gobat, R., Daddi, E., Magdis, G., et al. 2018, *Nature Astronomy*, 2, 239

Hayashi, M., Tadaki, K.-i., Kodama, T., et al. 2018, *ApJ*, 856, 118

Hopkins, P. F., Hernquist, L., Cox, T. J., Keres, D., & Wuyts, S. 2009, *ApJ*, 691, 1424

Ichikawa, T., Kajisawa, M., Yamada, T., et al. 2010, *ApJ*, 709, 741

Illingworth, G., Magee, D., Bouwens, R., et al. 2016, *ArXiv e-prints*, arXiv:1606.00841

Illingworth, G. D., Magee, D., Oesch, P. A., et al. 2013, *ApJS*, 209, 6

Jiao, Q., Zhao, Y., Lu, N., et al. 2019, *ApJ*, 880, 133

Kajisawa, M., Morishita, T., Taniguchi, Y., et al. 2015, *ApJ*, 801, 134

Kauffmann, G., Heckman, T. M., White, S. D. M., et al. 2003, *MNRAS*, 341, 33

Khochfar, S., & Silk, J. 2006, *ApJL*, 648, L21

Kocevski, D. D., Barro, G., Faber, S. M., et al. 2017, *ApJ*, 846, 112

Kriek, M., Conroy, C., van Dokkum, P. G., et al. 2016, *Nature*, 540, 248

Lianou, S., Xilouris, E., Madden, S. C., & Barmby, P. 2016, *MNRAS*, 461, 2856

Luo, B., Brandt, W. N., Xue, Y. Q., et al. 2017, *The Astrophysical Journal Supplement Series*, 228, 2

Man, A. W. S., Lehnert, M. D., Vernet, J. D. R., De Breuck, C., & Falkendal, T. 2019, *A&A*, 624, A81

Marchesini, D., van Dokkum, P. G., Förster Schreiber, N. M., et al. 2009, *ApJ*, 701, 1765

Mármol-Queraltó, E., Trujillo, I., Pérez-González, P. G., Varela, J., & Barro, G. 2012, *MNRAS*, 422, 2187

McDermid, R. M., Alatalo, K., Blitz, L., et al. 2015, *MNRAS*, 448, 3484

Morishita, T., & Ichikawa, T. 2016, *ApJ*, 816, 87

Morishita, T., Ichikawa, T., & Kajisawa, M. 2014, *ApJ*, 785, 18

Morishita, T., Ichikawa, T., Noguchi, M., et al. 2015, *ApJ*, 805, 34

Morishita, T., Abramson, L. E., Treu, T., et al. 2017, *ApJ*, 835, 254

—. 2019, *ApJ*, 877, 141

Muzzin, A., Marchesini, D., Stefanon, M., et al. 2013, *ApJ*, 777, 18

Naab, T., Johansson, P. H., & Ostriker, J. P. 2009, *ApJL*, 699, L178

Naab, T., Johansson, P. H., Ostriker, J. P., & Efstathiou, G. 2007, *ApJ*, 658, 710

Newman, A. B., Ellis, R. S., Bundy, K., & Treu, T. 2012, *ApJ*, 746, 162

Nipoti, C., Treu, T., Auger, M. W., & Bolton, A. S. 2009, *ApJL*, 706, L86

Nipoti, C., Treu, T., Leauthaud, A., et al. 2012, *MNRAS*, 422, 1714

Oliphant, T. E. 2006, *A guide to NumPy*, Vol. 1 (Trelgol Publishing USA)

Oser, L., Ostriker, J. P., Naab, T., Johansson, P. H., & Burkert, A. 2010, *ApJ*, 725, 2312

Papadopoulos, P. P., Thi, W. F., & Viti, S. 2004, *MNRAS*, 351, 147

Papovich, C., Labbé, I., Quadri, R., et al. 2015, *ApJ*, 803, 26

Patel, S. G., van Dokkum, P. G., Franx, M., et al. 2013, *ApJ*, 766, 15

Peng, Y., Maiolino, R., & Cochrane, R. 2015, *Nature*, 521, 192

Poggianti, B. M., Calvi, R., Bindoni, D., et al. 2013, *ApJ*, 762, 77

Salpeter, E. E. 1955, *ApJ*, 121, 161

Semenov, V. A., Kravtsov, A. V., & Gnedin, N. Y. 2018, *ApJ*, 861, 4

Shen, S., Mo, H. J., White, S. D. M., et al. 2003, *MNRAS*, 343, 978

Skelton, R. E., Whitaker, K. E., Momcheva, I. G., et al. 2014, *ApJS*, 214, 24

Smith, M. W. L., Gomez, H. L., Eales, S. A., et al. 2012, *ApJ*, 748, 123

- Solomon, P. M., & Vanden Bout, P. A. 2005, *ARA&A*, 43, 677
- Speagle, J. S., Steinhardt, C. L., Capak, P. L., & Silverman, J. D. 2014, *ApJS*, 214, 15
- Szomoru, D., Franx, M., van Dokkum, P. G., et al. 2010, *ApJL*, 714, L244
- Tacconi, L. J., Genzel, R., Saintonge, A., et al. 2018, *ApJ*, 853, 179
- Talia, M., Pozzi, F., Vallini, L., et al. 2018, *MNRAS*, 476, 3956
- Taylor, E. N., Franx, M., Glazebrook, K., et al. 2010, *ApJ*, 720, 723
- Thomas, D., Maraston, C., & Bender, R. 2003, *MNRAS*, 339, 897
- Tomczak, A. R., Quadri, R. F., Tran, K.-V. H., et al. 2014, *ApJ*, 783, 85
- Treu, T., Ellis, R. S., Liao, T. X., & van Dokkum, P. G. 2005, *ApJL*, 622, L5
- Trujillo, I., Conselice, C. J., Bundy, K., et al. 2007, *MNRAS*, 382, 109
- Trujillo, I., Ferreras, I., & de La Rosa, I. G. 2011, *MNRAS*, 415, 3903
- Trujillo, I., Förster Schreiber, N. M., Rudnick, G., et al. 2006, *ApJ*, 650, 18
- Valentinuzzi, T., Fritz, J., Poggianti, B. M., et al. 2010, *ApJ*, 712, 226
- Van Der Walt, S., Colbert, S. C., & Varoquaux, G. 2011, *Computing in Science & Engineering*, 13, 22
- van der Wel, A., Franx, M., van Dokkum, P. G., et al. 2014, *ApJ*, 788, 28
- van Dokkum, P. G., Abraham, R., Merritt, A., et al. 2015, *ApJL*, 798, L45
- van Dokkum, P. G., Franx, M., Kriek, M., et al. 2008, *ApJL*, 677, L5
- van Dokkum, P. G., Whitaker, K. E., Brammer, G., et al. 2010, *ApJ*, 709, 1018
- Wagg, J., Wilner, D. J., Neri, R., Downes, D., & Wiklind, T. 2006, *ApJ*, 651, 46
- Wei, A., Downes, D., Henkel, C., & Walter, F. 2005, *A&A*, 429, L25
- Wei, A., Henkel, C., Downes, D., & Walter, F. 2003, *A&A*, 409, L41
- Wellons, S., Torrey, P., Ma, C.-P., et al. 2016, *MNRAS*, 456, 1030
- Whitaker, K. E., Rigby, J. R., Brammer, G. B., et al. 2014, *ApJ*, 790, 143
- Williams, C. C., Giavalisco, M., Cassata, P., et al. 2014, *ApJ*, 780, 1
- Williams, J. P., de Geus, E. J., & Blitz, L. 1994, *ApJ*, 428, 693
- Wisnioski, E., Mendel, J. T., Förster Schreiber, N. M., et al. 2018, *ApJ*, 855, 97
- Wu, P.-F., van der Wel, A., Bezanson, R., et al. 2018, *ApJ*, 868, 37